FLOW AND HEAT TRANSFER CHARACTERISTICS OF THERMOCAPILLARY CONVECTION OF HIGH PRANDTL NUMBER FLUID IN CYLINDRICAL BRIDGE

K. Nishino[1], E. A. Matida[1] and S. Yoda[2]

[1]Yokohama National University, 79-5 Tokiwadai, Hodogaya-ku, Yokohama 240-8501, Japan
[2]National Space Development Agency of Japan, 2-1-1 Sengen, Tsukuba City, 305-8505, Japan

The onset of oscillation of thermocapillary convection (or Marangoni convection) in cylindrical liquid bridge has been a target of extensive studies from view points not only of the material processing in microgravity but also of the fundamental instability mechanism in this unique convection. The uniqueness lies in the facts (1) that the convection is driven by the surface tension gradient present along the liquid-gas interface, (2) that there is a strong coupling between fluid motion and fluid temperature, and (3) that the liquid surface may be deformed statically and dynamically. The last feature, particularly the dynamic surface deformation (DSD, hereafter), has not been paid enough attention so far even though some recent studies (e.g., Masud et al. 1997 and Kamotani & Ostrach 1998) have pointed out possible roles of DSD in the mechanism of onset of oscillation.

This report describes the results gained in experimental work done at Heat Transfer Laboratory of Yokohama National University in the period from April 2000 through March 2001. The work consists of (1) measurement of static surface deformation caused by the onset of convection, (2) simultaneous observation of flow patterns and DSDs of oscillatory convection, and (3) evaluation of heat loss from the free liquid surface. All of these are aiming at obtaining direct experimental clues that support the importance of DSD in the onset of oscillation of thermocapillary convection in cylindrical liquid bridge.

1. MEASUREMENT OF STATIC SURFACE DEFORMATION

1.1 Introduction

Deformability of the free liquid surface presents a unique character to the thermocapillary convection in a liquid bridge. The deformation takes place both statically and dynamically. The static deformation refers to the time-independent displacement of the free surface caused by (1) the hydrostatic forces such as the gravity and centrifugal force, (2) the change of surface tension due to variations of surface temperature, and (3) the change of static pressure field due to convection. Once the thermocapillary convection becomes oscillatory or chaotic, the free surface may be deformed time-dependently, hence showing dynamic surface deformation.

The static surface deformation caused by the hydrostatic forces can be evaluated by solving the Laplace equation that describes the force balance at the free surface. Its mathematical treatment is found in the book written by Antar & Nuotio-Antar (1993). On the other hand, the evaluation of the static surface deformation due to the steady thermocapillary convection requires the solution of the Navier-Stokes equations under the boundary conditions assigned at the deformable free surface. Some calculations for the static surface deformation caused by the steady thermocapillary convection in liquid bridge are reported by Kozhoukharova & Slavchev (1986) and Li et al. (1993). Shevtsova et al. (1997) and

Kawamura (2000) have developed numerical schemes for calculating dynamic surface deformation as well.

All the previous computational studies mentioned above lack in quantitative comparison with experimental data. This is simply because there is no reliable experimental data available even for static surface deformations due to the changes of surface tension and static pressure field. Nishino et al. (1999) developed a microscopic imaging technique for measuring surface deformation with sub-micron accuracy. The technique is verified by the direct comparison with the laser-focusing displacement meter having an accuracy of 0.05 μm. As the microscopic imaging technique can measure, by acquiring just a single image, the entire shape along an edge of the liquid bridge (i.e., the shape between the disks), it is suitable for the measurement of static surface deformation. This feature is exploited here in measuring static surface deformations that are caused by the onset of steady thermocapillary convection in silicone-oil bridges.

1.2 Calculation of Meniscus Shape

In this section, a mathematical formulation for meniscus shapes of convection-free liquid bridges is presented with reference to the approach described by Antar & Nuotio-Antar (1993).

In the absence of system rotation, there is a hydrostatic force balance in the liquid bridge:

$$p = -\rho g z + c \,, \tag{2.1}$$

where p is the liquid pressure, ρ the liquid density, g the acceleration of gravity, z the vertical coordinate and c an arbitrary constant. At the liquid free surface, the Laplace's condition gives the following relation:

$$p_v - p = \sigma\left(\frac{1}{R_1} + \frac{1}{R_2}\right), \tag{2.2}$$

where p_v is the pressure of ambient gas, σ the surface tension, and R_1 and R_2 the two principal radii of curvature measured from the gas side toward the liquid surface. The sum of these two principal radii for any surface shape function, $S = f(r, \theta, z)$, is given by

$$\frac{1}{R_1} + \frac{1}{R_2} = \pm\vec{\nabla}\cdot\frac{\vec{\nabla}f}{\sqrt{1+\left(\vec{\nabla}f\right)^2}} \tag{2.3}$$

From Eqs. (2.1)-(2.3), the following free-surface equation results:

$$\vec{\nabla}\cdot\frac{\vec{\nabla}f}{\sqrt{1+\left(\vec{\nabla}f\right)^2}} = \pm\left(\frac{\rho}{\sigma}gz + \frac{c}{\sigma}\right) = bz + k \,, \tag{2.4}$$

where $b = \pm\rho g/\sigma$ and $k = \pm c/\sigma$ with p_v included in c. Note that the negative sign should be adopted for the calculation of liquid bridge surfaces described below.

For an axisymmetric liquid surface, the free-surface equation, Eq. (2.4), can be transformed into the following set of two equations (Antar & Nuotio-Antar 1993):

$$\frac{d^2r}{ds^2} = -\frac{dz}{ds}\left(-bz - k - \frac{1}{r}\frac{dz}{ds}\right), \tag{2.5}$$

$$\frac{d^2z}{ds^2} = -\frac{dr}{ds}\left(-bz - k - \frac{1}{r}\frac{dz}{ds}\right), \tag{2.6}$$

where s is the parameter measured along the liquid surface (refer to Fig. 1-1). These equations are integrated from the boundary conditions at $z = 0$ (i.e., at the lower disk surface). The boundary conditions given here are

$$r = D/2, \tag{2.7}$$

$$dz/dr = \tan\beta_0. \tag{2.8}$$

The first boundary condition corresponds to the requirement that the liquid bridge is pinned at the lower disk edge, while the second boundary condition assigns the macroscopic contact angle, β_0. It is important to note that the value of β_0 is not determined explicitly but determined after iterative calculations for meniscus shape. The iteration is repeated with varying the value of β_0 until the integrated meniscus shape reaches the upper disk edge, the second requirement as depicted in Fig. 1-1. The liquid volume is specified by the value of k.

The meniscus shapes calculated thus for various volume ratios, V/V_0, are presented in Fig. 1-2. The calculation conditions are summarized in Table 1-1. As anticipated, the meniscus shape is not axially flat even for V/V_0 = 100%, showing an outward deformation near the lower disk and an inward deformation near the upper disk, both being due to the gravity.

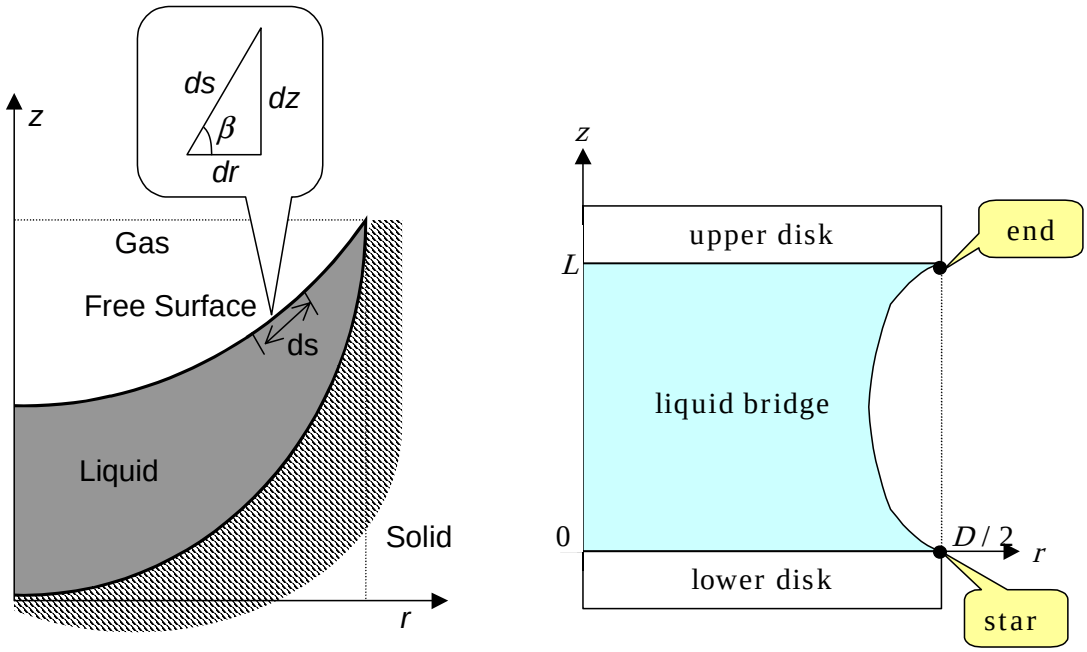

Fig. 1-1 Definition of coordinate system and boundary conditions.

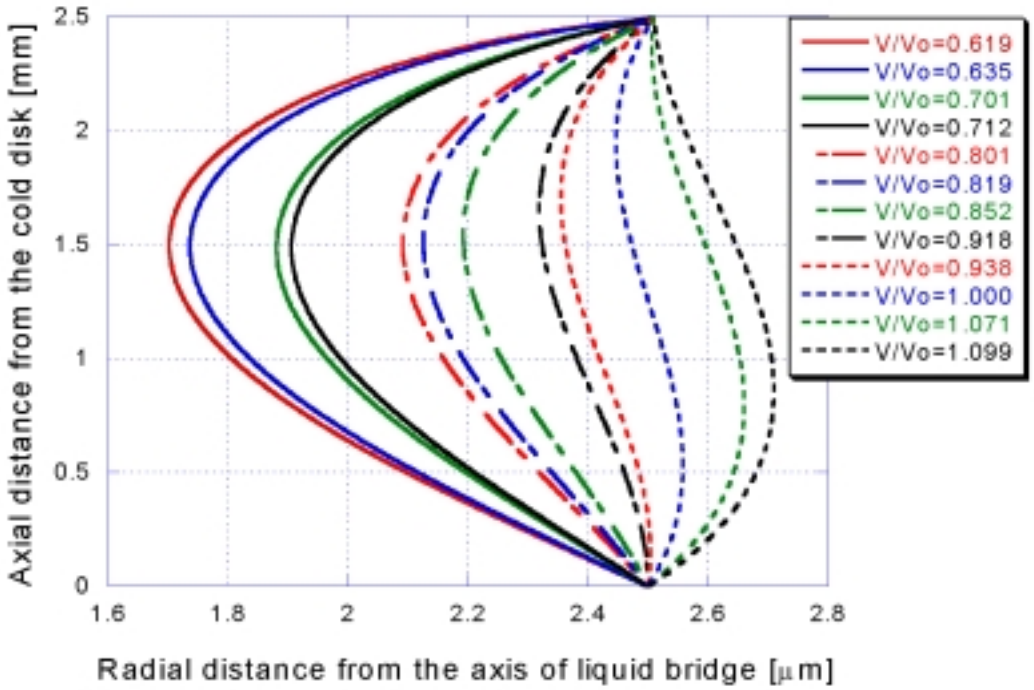

Fig. 1-2 Meniscus shapes calculated for various volume ratios.

Table 1-1 Conditions for meniscus shape calculations.

Disk diameter, D	5.0 mm
Aspect ratio, L/D	0.5
Volume ratio, V/V_0	0.62-1.10
Working fluid and its physical properties	Silicone oil
	Kinematic viscosity: 5 cSt
	Surface tension: 0.0197 N/m
	Density: 915 kg/m^3

1.3 Measurement

The meniscus shape and static surface deformation caused by the onset of thermocapillary convection is measured with the microscopic imaging technique as depicted in Fig. 1-3. A high-definition CCD camera with 1920×1035 sensor elements is used for image acquisition. Illumination is given from the back of the liquid bridge so that the liquid bridge is viewed as dark area in the FOV of the camera. To measure static surface deformation for a particular convection condition (or Marangoni number), a set of three images are acquired as shown in Fig. 1-4; (a) an image of the disks without liquid, (b) an image of the liquid bridge in the presence of convection, and (c) an image of the liquid bridge in the absence of convection. As demonstrated here, the wide FOV of the high-definition CCD camera permits viewing of an entire profile of the liquid bridge edge between the disks by the single image acquisition. The disk image without liquid is for determining the disk positions, while the two liquid-bridge images are for measuring displacement of the liquid-bridge edge.

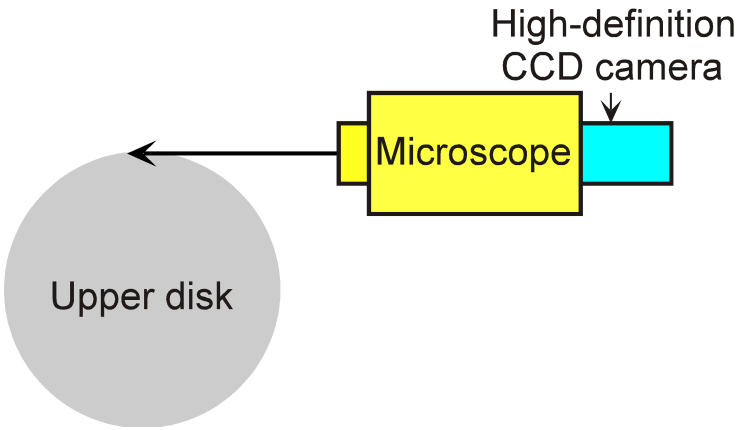

Fig. 1-3 Schematic of microscopic imaging technique.

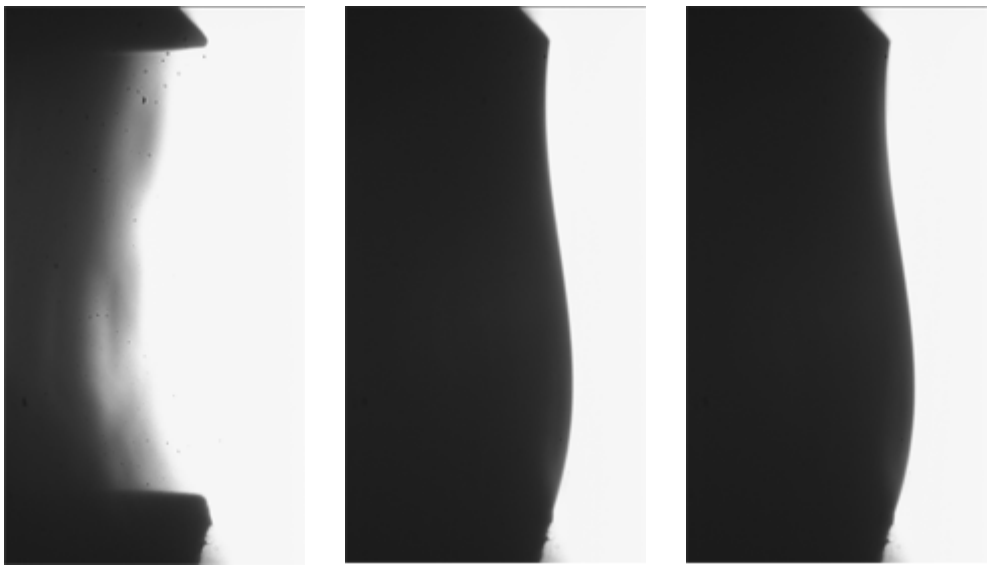

(a) (b) (c)

Fig. 1-4 Acquired images (a) without liquid, (b) with thermocapillary convection (*Ma* = 10,000), and (c) without thermocapillary convection.

The measurement conditions are summarized in Table 1-2. The measured liquid bridge shapes for two pairs: one is for *Ma*=0 and 10,000 and the other for *Ma*=0 and 3,000 are shown in Fig. 1-5. Note that these values of *Ma* are nominal ones and more precise values are listed in Table 1-2. As expected, the magnitude of surface deformation due to onset of Marangoni convection is larger for *Ma*=10,000 than for 3,000. The deformation near the lower (cold) disk is positive (outward) and that near the upper (hot) disk is negative (inward), consistent with the increase of static pressure due to the convection near the lower disk and with its decrease near the upper disk.

Table 1-2 Conditions for the measurement of static surface deformation.

Upper (or hot) disk diameter, D_h Lower (or cold) disk diameter, D_c	5.00 mm 5.0488 mm
Aspect ratio, L/D_h	0.5 (L=2.5 mm)
Volume ratio, V/V_0	1.048172
Mean temperature, $(T_h+T_c)/2$	30±0.25 °C
Working fluid and its physical properties (at 30 °C)	Silicone oil Density: 911 kg/m^3 Kinematic viscosity: 4.6×10^{-6} m^2/s (5.0×10^{-6} m^2/s at 25 °C) Surface tension: 0.0194 N/m Temperature coefficient of surface tension: -0.061×10^{-3} N/(m·K) Thermal diffusivity: 7.45×10^{-8} m^2/s (at 25 °C) Prandtl number: 67.1 (at 25 °C)
Temperature difference zero temperature difference case low temperature difference case high temperature difference case	 $\Delta T=T_h-T_c$=0 °C (Ma=0) $\Delta T=T_h-T_c$=7 °C (Ma=3,420) $\Delta T=T_h-T_c$=22.5 °C (Ma=10,990)

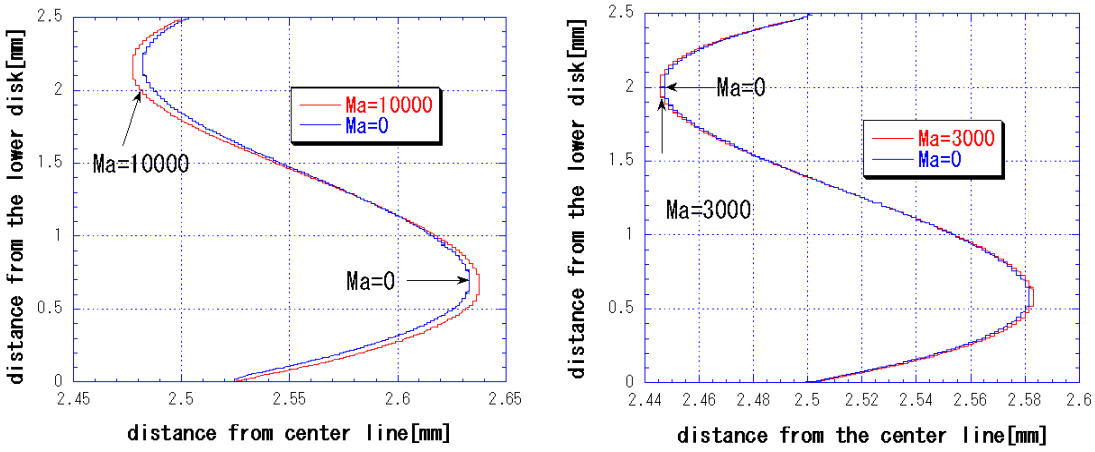

(a) (b)

Fig. 1-5 Liquid bridge shapes measured for (a) Ma=0 and 10,000, and (b) Ma=0 and 3,000

Surface deformation is quantified by subtracting the surface position for Ma=0 from that for Ma=10,000 or 3,000. The results are plotted in Fig. 1-6. Obviously, the surface deformation for Ma=10,000 is significantly larger than that for Ma=3,000. The peak deformation near the upper disk for Ma=10,000 is -5 μm, while that near the lower disk is +8 μm. The peak deformations for Ma=3,000 are about ±3 μm.

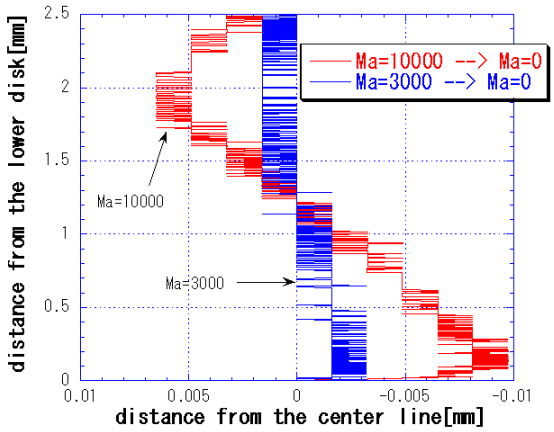

Fig. 1-6 Surface deformations due to the onset of Marangoni convection

The shape of liquid bridge measured presently for *Ma*=10,000 is compared with that calculated numerically by Kawamura (2001) in Fig. 1-7(a). The shape for *Ma*=0 measured is included for reference. The static surface deformations calculated from the shapes of liquid bridge are presented in Fig. 1-7(b). As recognized in this figure, there is an appreciable quantitative discrepancy in the surface deformation between the present experiment and the numerical calculation, although qualitatively both experiment and numerical calculation provide a similar profile. The peak deformation near the upper disk is -5 μm experimentally while -2 μm numerically, and the peak deformation near the lower disk is +8 μm experimentally while +2 μm numerically. The reason for this discrepancy is not fully understood yet, but one possibility is a leakage of very small amount of liquid through the edge of the lower disk in the experiment. It is actually observed in some images of the liquid bridge that the contact point, which is assumed to be pinned to the edge of the lower disk in the numerical calculation, is displaced slightly downward along the side surface of the disk edge when Marangoni convection is commenced. This issue has to be examined in full detail in the future.

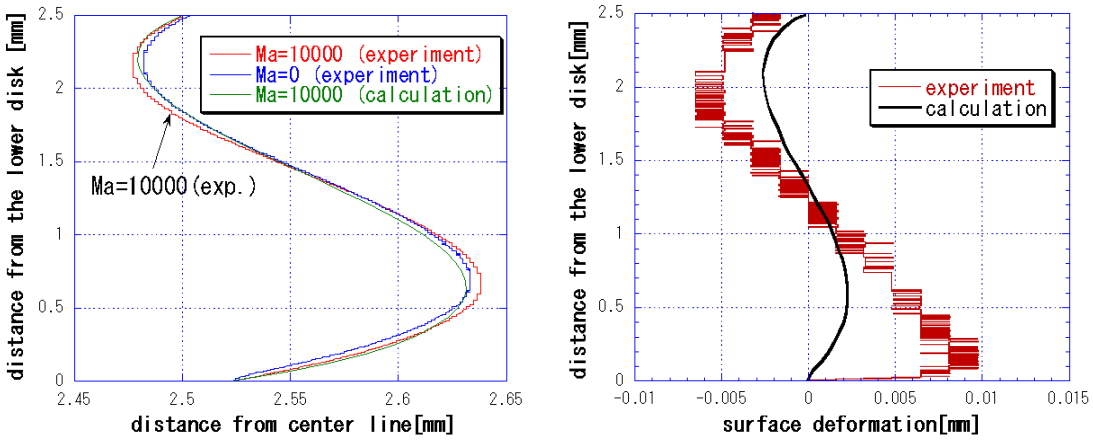

(a) (b) *Ma*=10,000

Fig. 1-7 Comparison of liquid bridge shape and surface deformation between the present experiment and a numerical calculation by Kawamura (2001).

1.4 Conclusions

The shape of liquid bridge and its static deformation caused by the onset of thermocapillary convection is measured by using a microscopic imaging technique developed in this project. It is shown that the thermocapillary convection causes a positive (outward) deformation near the lower (cold) disk while it causes a positive (inward) deformation near the upper (hot) disk. This qualitative tendency is consistent with the variation of the static pressure field by the onset of thermocapillary convection; i.e., the local pressure near the lower disk increases while that near the upper disk decreases. The magnitude of deformation is larger for higher temperature difference (or Marangoni number). For *Ma*=10,000 nominally, the outward deformation near the lower disk is about +8 μm while the inward deformation near the upper disk is about -5 μm. The measured surface deformation is compared with a numerical computation by Kawamura (2001). Although the two provide a qualitatively similar profile, there is an appreciable discrepancy between the two. The reason for it is not yet clear at this stage, but some experimental problems such as leakage of very small amount of liquid are suspected, which must be examined in full detail.

2. SIMULTANEOUS OBSERVATION OF FLOW PATTERN AND DSD IN THE HOT CORNER

2.1 Introduction

Liquid bridges suspended between two coaxial disks maintained at different temperatures are the simplified models of the floating zone method considered for manufacturing contamination-free semiconductor crystals for power transistors. As schematically shown in Fig. 2-1, the temperature gradient present along the surface of the liquid bridge causes a surface tension gradient. It generates a thermocapillary convection (or Marangoni convection) that circulates from the region of low surface tension (usually high-temperature region) toward the region of high surface tension (usually low-temperature region). In the liquid bridge configuration, a toroidal flow pattern appears as a result of the surface flow and the return flow. The flow pattern remains steady and axisymmetric as long as the temperature difference (and hence the driving force) is below a certain critical value. Above the critical value, the flow goes through a transition to become oscillatory and asymmetrical about the axis, the flow state that is known to be detrimental to the growth of defect-free semiconductor crystals.

Some recent studies (e.g., Masud et al. 1997 and Kamotani & Ostrach 1998) suggest that the dynamic surface deformation of liquid bridge can play an important role in the transition mechanisms mentioned above. This suggestion is based on the experimental findings that the transition conditions for a wide range of liquid bridge conditions are correlated well with a non-dimensionalized parameter representing “deformability” of liquid bridge surface. However, the findings are contrasted with the assumption made in the linear stability analysis and direct numerical simulation, both of which assume that DSD is of negligible importance in the governing equation. This contradiction is left unsolved so far and its complete solution needs extensive experiments under wider range of liquid bridge conditions, which are possible only in the long-period microgravity environment provided by the International Space Station that will be available in the near future.

The present study aims at obtaining in the ground experiments some direct evidence on the role of DSD in the oscillatory thermocapillary convection in the liquid bridge. This is done by performing simultaneous observation of flow patterns and DSDs in the flow region near the tip of the hot disk (denoted as "hot corner" hereafter), the region that is considered to be responsible for triggering the onset of oscillation. A microscopic imaging displacement

meter developed in the Heat Transfer Laboratory at Yokohama National University through the cooperative research contract with National Space Development Agency of Japan (NASDA) is used to measure the oscillatory displacement of the free surface in the hot corner. This measurement is synchronized with flow visualization based on the tracer method to observe associated flow patterns in the hot corner. Temperature information is also gained through thermometry with a fine thermocouple probe placed in the hot corner. The information gained will be integrated into a phenomenological model that can explain an oscillation sequence of observed quantities (i.e., flow pattern, DSD and temperature) and their role in the sustenance of oscillation.

2.2 Experimental facility and method

2.2.1 Liquid bridge

The working fluid used in the present experiments is 5-cSt silicone oil (KF96-5cSt) available from Shin-etsu Chemical Industries Co. Ltd. Its physical properties at 20 °C are summarized in Table 2-1.

Table 2-1 Physical quantities of the working fluid (KF96-5cSt).

density, ρ	915 kg/m^3
kinematic viscosity, ν	5×10^{-6} m^2/s
surface tension, σ	19.7×10^{-3} N/m
temperature coefficient of surface tension,	-0.061×10^{-3} N/(m·K)

Figure 2-1 shows the flow configuration. The liquid bridge is suspended in the gap between two coaxial rods 5 mm in diameter. The gap length is 2.5 mm, giving an aspect ratio, $Ar=L/d$, of 0.5, where L is the gap length and d the rod diameter. The working fluid is injected into the gap by using a precision syringe connected to a micrometer head. The volume of injected fluid, V, is varied between 100% to 110% of the volume of the gap (i.e., V/V_0=100, 107 and 110%, where V_0 is the volume of the gap). The volume ratio of 107% is chosen because it gives an axially straight meniscus shape near the hot corner and thus provides a good optical access into the hot corner.

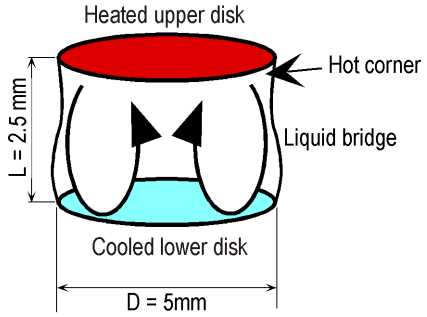

Fig. 2-1 Thermocapillary convection in a liquid bridge.

The rods are made of aluminum alloy. The upper rod is heated with a ribbon heater, while the lower rod is cooled with a Peltier element. The rod temperature is measured with a thermocouple 50 μm in wire diameter. Five pairs of thermocouple are imbedded along the axis of each rod, with the fifth one imbedded 2.5 mm from the rod end surface. Since the temperature gradient along the rod is small, the temperature difference between the end surfaces of upper and lower rods (referred to as "disk temperature difference" hereafter), ΔT, is defined as a temperature difference between the fifth thermocouples. The critical temperature difference, ΔT_c, for each volume ratio is determined by detecting carefully the onsets of temperature oscillation and DSD. The critical temperature differences determined are summarized in Table 2-2. In these experiments, the temperature of the lower rod is maintained approximately at 20 °C and the temperature of the upper rod is increased very slowly.

Table 2-2. Critical disk temperature differences, ΔT_c, for different volume ratios.

V/V_0	ΔT_c
100%	35.7 K
107%	33.5 K
110%	30.6 K

2.2.2 Microscopic imaging displacement meter

Dynamic surface displacement is measured with a microscopic imaging displacement meter. This technique is based on (1) back-lighting of the liquid bridge with a white light source and (2) microscopic-imaging of the edge of the liquid surface. A Nikon stereomicroscope and a NTSC-based B&W CCD camera are used to acquire microscopic images of the liquid surface. The FOV is 200×200 μm^2 for a CCD array having 640×480 cells, achieving a cell resolution of 0.37 μm/pixel. As shown in Fig. 2-2(b), the liquid bridge appears dark in the white background.

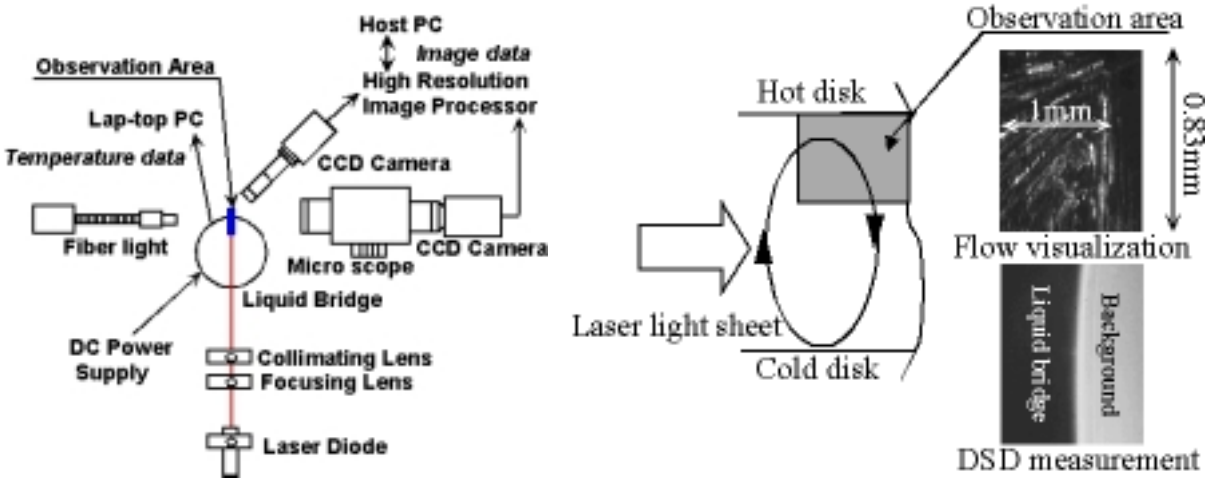

(a) (b)

Fig. 2-2 DSD measurement and flow visualization of the hot corner: (a) the present optical set-up and (b) images acquired in flow visualization and DSD measurement.

The position of the liquid free surface is determined as a point having maximum slope in gray-level profile along each horizontal TV line. In order to improve S/N ratio of this position measurement, averaging of ten positions determined from neighboring horizontal lines is taken. As a result, the resolution of the present displacement measurement is improved to be about 0.05 μm, which is high enough to resolve an extremely small magnitude of DSD observed near ΔT_c. The accuracy of the microscopic imaging displacement meter is verified by the direct comparison with a commercially available laser-focusing displacement meter having a resolution of 0.05 μm. More details about the technique can be found in Nishino et al. (1999).

2.2.2 Flow visualization

A conventional tracer method is used for visualization of flow patterns in the hot corner of the liquid bridge (Fig. 2-2). Polystyrene particles, 20 μm in diameter and 1.07×10^3 kg/m^3 in density, are chosen as tracer particles. A diode laser emitting a sheet of 685-nm light with 28-mW power is used together with two cylindrical lenses, which are placed in the beam path to generate a laser light sheet 2.9 mm in height and 90 μm in thickness at the observation area. As shown in Fig. 2-2(a), a B&W CCD camera is placed at a forward angle so that there is no hidden region of the hot corner that would otherwise be generated by the effect of light refraction at a curved free surface of the liquid bridge. In the present experiment, a forward angle of 45 degrees is adopted as a result of ray-tracing calculations based on Snell's law of light refraction. In general, the angle should be small in order to eliminate hidden regions, while it should be large (as close to 90 degrees as possible) to minimize the perspective effect due to inclined observation. The present angle is chosen as a compromise of these two requirements. The resultant size of FOV is 1.0 mm horizontally and 0.83 mm vertically as indicated in Fig. 2-2(b).

The two CCD cameras, one for DSD measurement and the other for flow visualization, are synchronized with each other to allow simultaneous image acquisition by a high-speed image processor. The image acquisition rate is 60 TV fields per second and consecutive TV fields for about 30 s (i.e., 1,800 TV fields for each camera) are digitized. An example of flow visualization images is given in Fig. 2-2(b). Note that the white lines seen in the image are the particle streaks generated during an exposure time of 1/60 s. In some experiments, simultaneous temperature measurement is made by using a fine thermocouple probe placed in the hot corner. A time-marking system with a strobescope is used to establish time registration between image acquisition and temperature sampling.

2.3 Results and discussion

Figure 2-3 shows a DSD signal and associated flow patterns at those phases marked as “A” to “H” in the DSD signal. The sign of DSD is defined positive if the deformation is outward and vice versa. The volume ratio is 107% and the disk temperature difference is ΔT_c+5 °C. The DSD measurement was taken at a location 48 μm from the hot disk. To facilitate understanding of the flow patterns, a schematic drawing is added in the figure. The flow patterns and DSD signal may be interpreted as follows:

(1) Phases A-B: The return flow (abbreviated as RF, hereafter) toward the hot corner is curved and along the hot disk surface. As anticipated from such flow patterns, the magnitude of RF quantified by the length of each streakline at these phases is found to be smaller than that at opposite phases (E-F).

(2) Phases C-F: The pattern of RF becomes straight and appears to be sucked strongly into HC. This is particularly evident at Phase E that is corresponding to a negative peak deformation of liquid surface. Although not apparent from still images

shown here, the motion images clearly indicate that the sucking of RF is associated with the temporal acceleration of the surface flow (abbreviated as SF, hereafter) near the hot corner.

(3) Phases G-H: Both RF and SF start to be decelerated so that a circulating zone discernible as closed streaklines is shifted toward the hot corner. The presence of similar circulating zone is found in the numerical simulation by Kamotani (2000). Note that the circulating zone is not observed well at around Phase E because of its positional shift toward the lower disk.

The present visualization and measurement has revealed that the liquid surface is deformed inward (or negatively) at oscillation phases when SF is temporally accelerated and RF is sucked straight into the hot corner. This suggests that the local static pressure decrease near the hot corner caused by the acceleration of SF is the reason for the inward surface deformation and sucking of RF.

The effect of the volume ratio on the phase relationship between flow patterns and DSD is shown in Fig. 2-4, where only the flow patterns corresponding to positive peak (or maximum) and negative peak (or minimum) surface deformations. For both volume ratios shown here, the phase relationship is generally the same as that for V/V_0=1.07 described above. This indicates that the same explanation of the phase relationship applies to the range of volume ratio studied here. Not shown here, there is the same phase relationship for a range of disk temperature difference, ΔT=(ΔT_c+1.7)-(ΔT_c+11) °C.

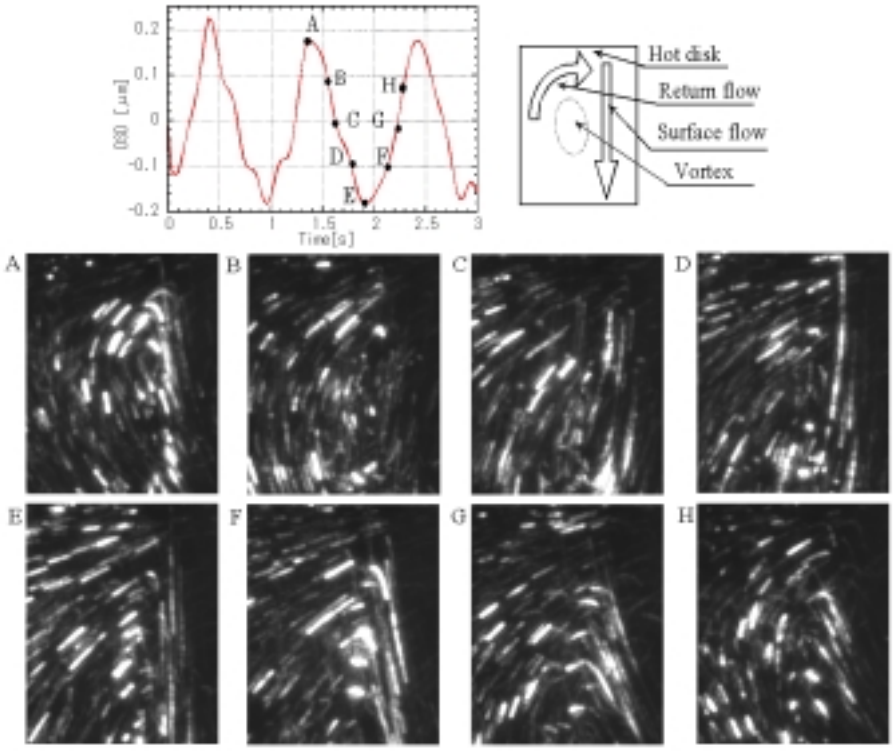

Fig. 2-3 Oscillation of DSD and associated flow patterns.

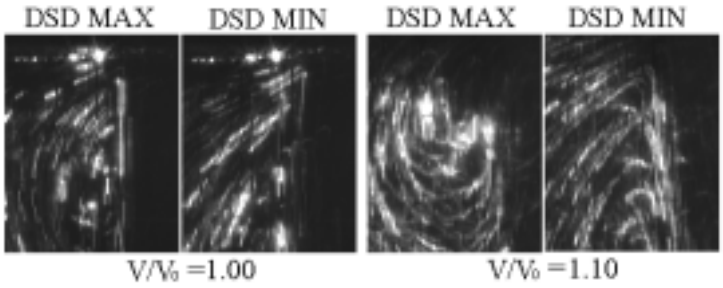

Fig. 2-4 Flow patterns at phases of maximum and minimum DSD for V/V_0=100% and 110 %.

Simultaneous temperature measurements for $\Delta T=\Delta T_c$+5.0 °C are taken at four thermocouple positions as summarized in Table 2-3. Also included is the position of DSD measurement.

Table 2-3 Thermocouple positions in simultaneous temperature measurements.

	#1	#2	#3	#4
Distance from UD	50 μm	500 μm	50 μm	400 μm
Depth from the surface	50 μm	100 μm	400 μm	600 μm
Distance from UD in DSD measurement	113 μm	48 μm	75 μm	48 μm

UD denotes the upper disk.

Figure 2-5 presents the signals of DSD and temperature for Position #3 along with streakline images at four representative phases marked as A to D in the DSD and temperature signal plots. It is evident that there is about 180-degree phase difference between DSD and fluid temperature: a peak positive deformation of liquid surface is associated with a minimum temperature of fluid in the hot corner and vice versa. This means that a slower and cooler fluid goes toward the hot corner at phases when SF is decelerated and DSD is thus outward while a faster and warmer fluid goes straight into the hot corner at phases when SF is accelerated and DSD is thus inward. Interestingly, the phase relationship mentioned here holds true for all thermocouple positions listed in Table 2-3

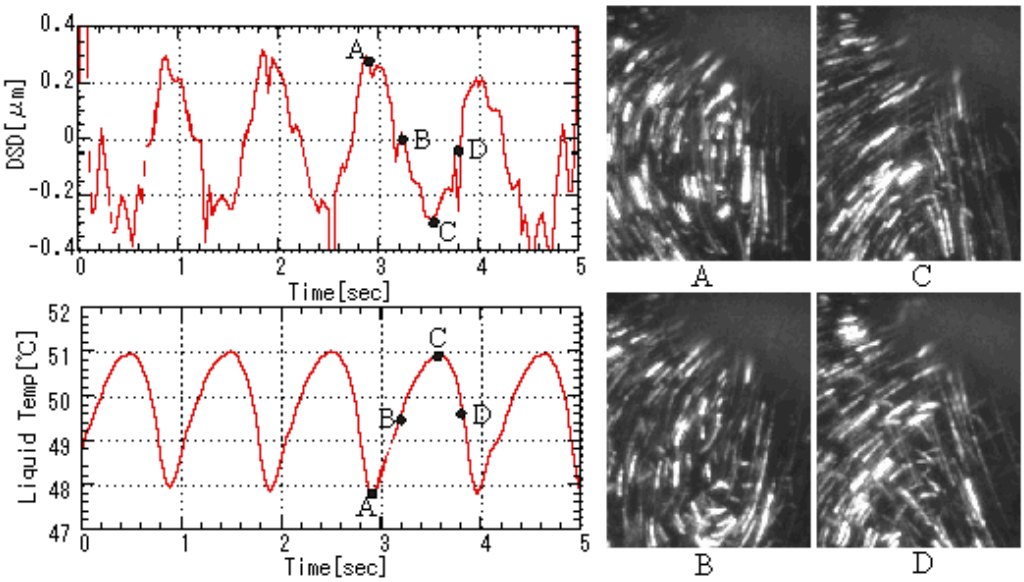

Fig. 2-5 Phase relationship among DSD, flow pattern and liquid temperature at Position #3.

2.4 Conclusions

Oscillation phenomena of thermocapillary convection in a liquid bridge of silicone oil are studied by performing simultaneous observation of the flow pattern and dynamic surface deformation in the corner region near the tip of the hot disk. Fluid temperature measurements are also taken with a fine thermocouple probe. The following conclusions may be drawn.

(1) The return flow in the hot corner is curved in streakline pattern and weak in magnitude at oscillation phases when the liquid surface near the hot corner is deformed outward (or positively). On the other hand, the return flow is straight toward the hot corner and strong in magnitude at oscillation phases when the liquid surface is deformed inward (or negatively).

(2) The same phase relation between flow patterns and surface deformations is observed for a range of volume ratio, 100-110%, and for a range of disk temperature difference, $\Delta T=(\Delta T_c+1.7)-(\Delta T_c+11)$ °C.

(3) The return flow patterns and associated dynamic surface deformations observed are most likely due to local static pressure variations caused by acceleration and deceleration of the surface flow in the hot corner.

(4) Temperature measurements have shown that the return flow is cooler when the surface deformation is outward and vice versa.

3. EVALUATION OF HEAT LOSS FROM THE FREE LIQUID SURFACE

3.1 Introduction

Floating zone is a containerless technique to produce a highly purified single crystal. Material is fed upwards through a ring heater and is molten locally in the region inside the ring. A single crystal is formed over this molten region. The characteristics of the flow inside the molten region influence the quality of the crystal. In order to optimize this crystal-growth process, the nature of the flow inside the molten liquid as well as the heat and mass transfer involved in the process must be well understood.

The floating zone can be simplified by a half-floating zone, where a liquid bridge is supported between two concentric disk rods, one disk being heated and the other being cooled. The gradual increase of the Marangoni number, $Ma = PrRe = |\sigma_T|D\Delta T/(\alpha\nu)$, or increase of the temperature difference between disks, $\Delta T = T_h - T_c$, will produce a steady thermocapillary convection that will become oscillatory (time dependent) above a critical Marangoni number, Ma_c , or critical temperature difference, ΔT_c .

Using linear stability theory, Smith & Davis (1983) and Kuhlmann & Rath (1993) have studied the instabilities (and their resulting forms) of dynamic thermocapillary liquid layers and cylindrical thermocapillary liquid bridges, respectively. In Kuhlmann & Rath's calculation, the influence of heat loss on the base state was destabilizing for low *Pr* numbers. However, for large *Pr* numbers, they have stated that the base state is always stabilized to hydrothermal waves by an increase of the Biot number ($Bi = h_{lbs}L/k_{oil}$, where h_{lbs} and k_{oil} are the average heat transfer coefficient at the liquid free surface and the thermal conductivity of the working fluid used, respectively). Fu & Ostrach's (1983) calculation, using a finite difference scheme to determine the flow and the temperature fields in cylindrical thermocapillary liquid bridges, indicates that the increasing of the free-surface heat loss influences the flow inside the liquid bridge, much more than the decreasing of it does. They also have shown that the temperature gradients increased at the top (near the hot disk rod) and in the middle of the free surface and decreased at the bottom of the free surface, when the heat loss is increased. More recently, Kamotani (2000) has stated that the increase of the heat loss has a destabilizing effect, resulting that there is still some controversies concerning the influence of the heat loss over the onset of oscillation. In the present report, some effort was given to the measurement of the heat loss from the liquid bridge surface of a half-floating zone to the surrounding air, under ground-based conditions. The heat loss from the liquid bridge is obtained indirectly by the subtraction of the measured heat fluxes through the upper and the lower disk rods.

3.2 Experimental apparatus

A schematic view of the experimental apparatus is shown in Fig. 3-1. The 10-cSt silicone oil (Shin-etsu Chemical Co., *Pr*=111 for 25 °C) liquid bridge is injected between two concentric aluminum alloy (52S, *k*=180 W/m/K) disk rods with 5.0 mm in diameter. The both disk rod ends have a sharp edge cut in 45 degrees. The cut part is coated with fluoride-liquid material (3M, FC-722) in order to avoid liquid bridge's frequent collapse during the experiments. 10-cSt silicone oil has extremely low evaporation rates in the temperature range (approximately from 20 to 130 °C) of the present experiment. Distance between disks can be varied by using a z-stage. A ribbon heater is used to heat the upper disk rod whereas the lower disk is cooled by a Peltier element. Five thermocouples (type K, 50 μm in diameter) are imbedded at the center of the upper disk rod and spaced equidistantly in the axial direction (5.0 mm pitch). Other five thermocouples are imbedded similarly in the lower disk rod.

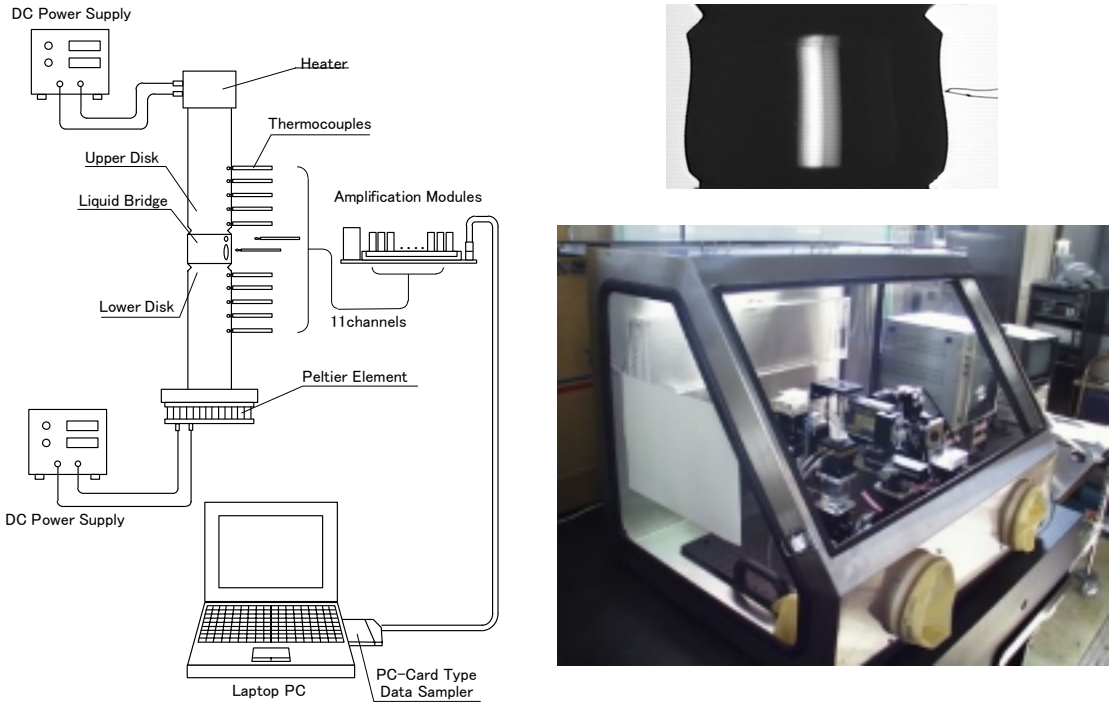

Fig. 3-1 Schematic view of the experimental apparatus.

Air temperature is measured with a thermocouple placed approximately 50 mm away from the liquid bridge. The onset of oscillation can be obtained by measuring the temperature of a single point near the surface of the liquid bridge. For this point measurement, a small thermocouple (type K, 13 μm in diameter) is used and placed approximately 50 μm outside the liquid bridge with an axial position of 0.4L from the upper disk as shown in Fig. 3-1, where L is the liquid bridge length.

The thermocouple electromotive force, emf, is amplified 1000 times, A/D converted by a PCMCIA card (Keyence, NR-110) and recorded in the hard-disk drive of a PC. Temperature can be obtained from the amplified signals by:

$$T = aE + b \tag{3.1}$$

Here, T [°C] is the temperature, E [V] is the amplified emf, a and b are coefficients obtained for each thermocouple (and correspondent amplifier) by calibration in a constant temperature box (Espec Corp., SU-220, –20 to 130 °C) as shown in Fig. 3-2.

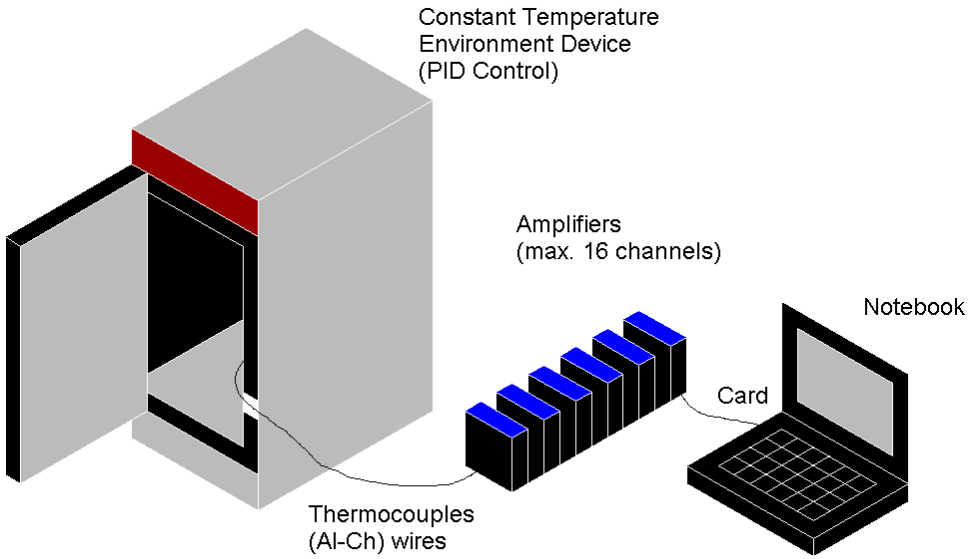

Fig. 3-2 Schematic view of thermocouple calibration system.

3.3 Determination of the onset of oscillation

The temperature difference between the disks is increased slowly with a rate of 0.03 °C/s. A steady thermocapillary convection is formed in the liquid bridge. The emfs of thermocouples are recorded simultaneously with a sampling rate of 20 Hz and a sampling length of about 7 min. After the recording, the data series of the surface temperature are filtered by a digital low-pass filter of 5 Hz cutoff. Above a critical temperature difference, ΔT_c, the steady thermocapillary convection will become oscillatory. The onset of oscillation can be determined by the start of oscillation of the liquid bridge surface temperature. In order to vary the natural convection around the liquid bridge, two plastic partition disks of 50.0 mm in diameter were placed 2.0 mm from the rod ends as shown in Fig 3-3.

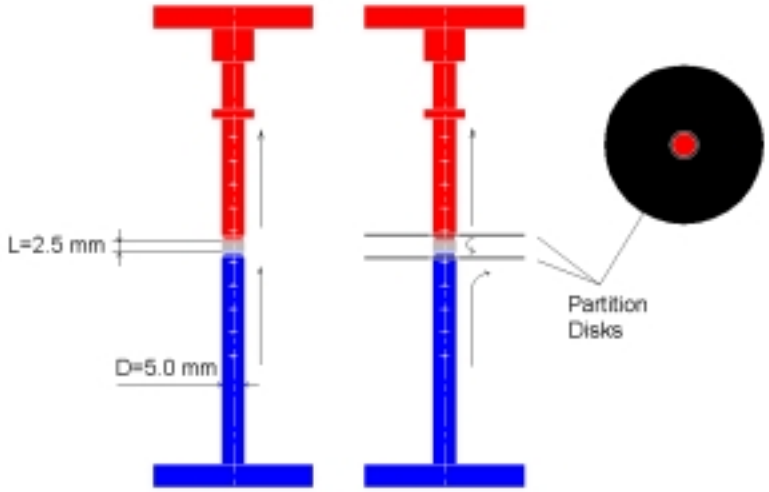

Fig. 3-3 Partial suppression of the natural convection around the liquid bridge.

Fig. 3-4 shows a typical plot of the onset of oscillation for two configurations (without and with the plastic partition disks) of a near flat liquid bridge (volume ratio $V/V_0 = 110\%$). Upper hot disk temperature, T_h, is shown in red solid line, the lower cold disk temperature, T_c, in blue dotted line and the liquid bridge surface temperature, T_{lbs}, in a green solid line. In this case the critical temperature difference, $\Delta T_c = T_h - T_c = 53.9$ and 69.4 °C (Ma_c = 22,776) for configurations with and without the partitions disks, respectively. Suppression of the natural convection seems to have a stabilizing effect concerning the onset of oscillation for nearly flat liquid bridges.

The partition disks seem not to affect significantly the onset of oscillation for slender liquid bridges (volume ratio $V/V_0 = 60.0\%$) as shown in Fig. 3-5. Fig. 3-6 shows the liquid bridge surface temperature, T_{lbs}, at steady supercritical conditions for configurations without and with the partition disks (volume ratio $V/V_0 = 110.0\%$). It is also shown in the figure, the correspondent FFT analysis of the T_{lbs}, indicating that the frequency of oscillation is faster when the partition disks are used.

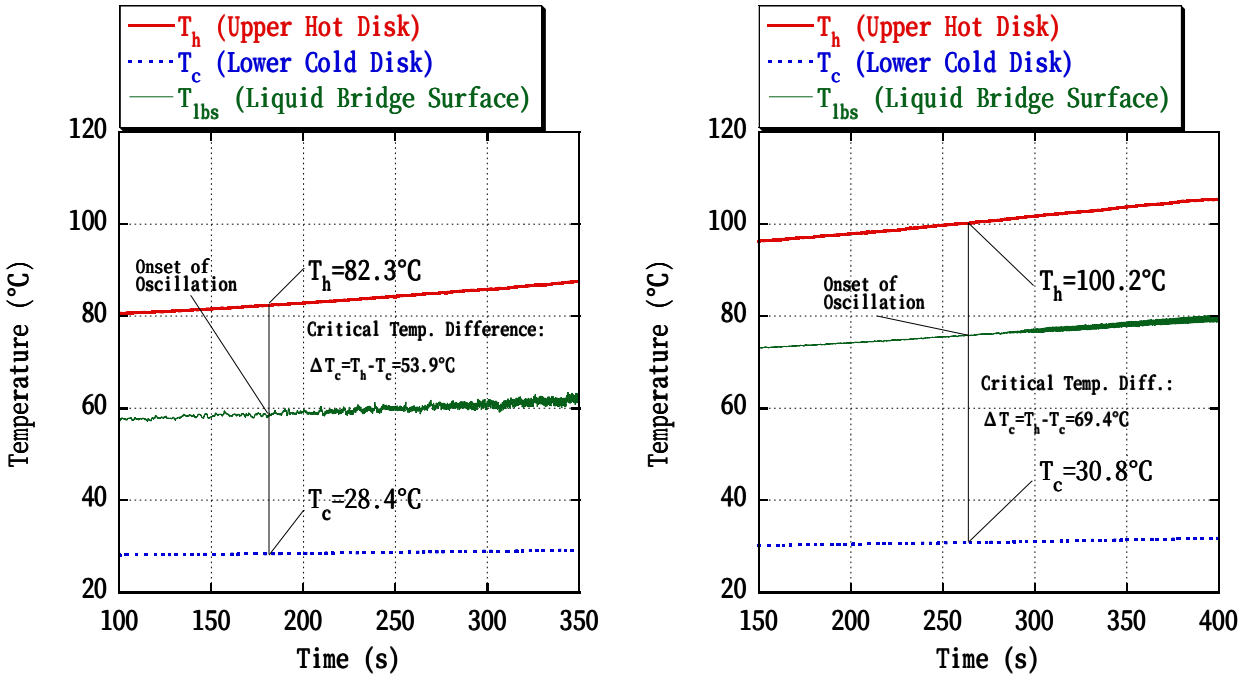

(a) without partition disks (b) with partition disks

Fig. 3-4 Typical onset of oscillation for nearly flat liquid bridges
(silicone oil, 10 cSt, $D = 5.0$ mm, $L = 2.5$ mm, $T_{ambient}$ =20.6 °C, $V/V_0 = 110\%$)

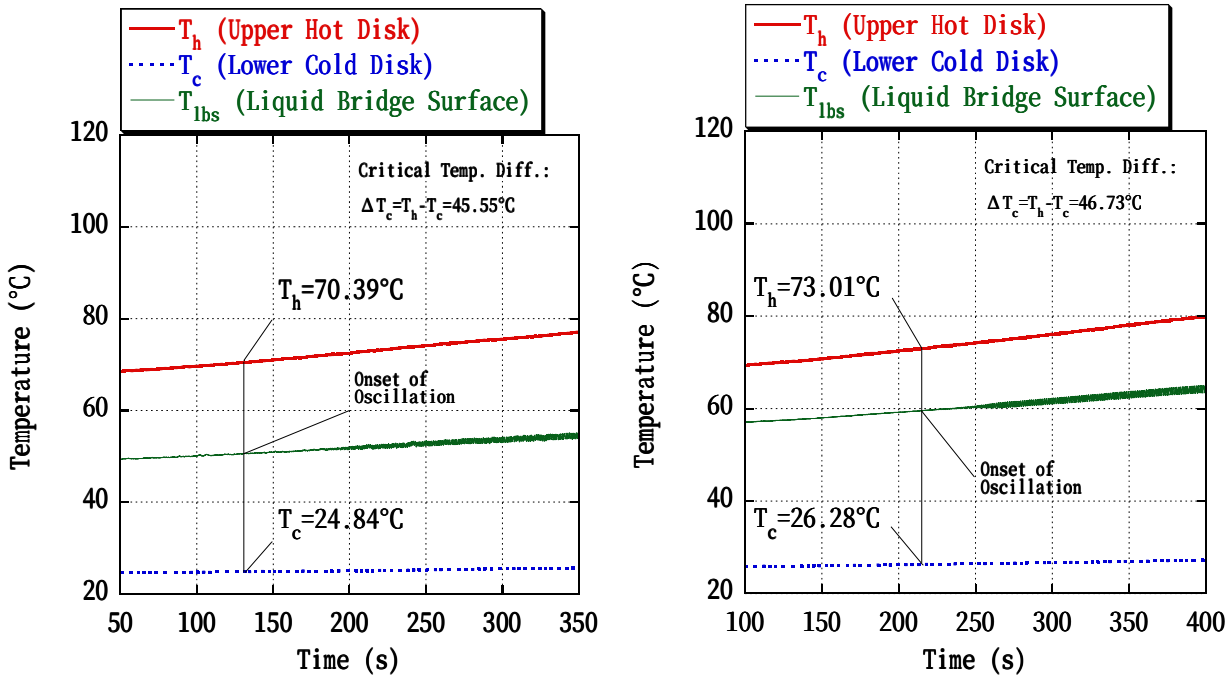

(a) without partition disks (b) with partition disks

Fig. 3-5 Typical onset of oscillation for slender liquid bridges
(silicone oil, 10 cSt, $D = 5.0$ mm, $L = 2.5$ mm, $T_{ambient,(a)} = 20.6$ °C, $T_{ambient,(b)} = 18.6$ °C, $V/V_0 = 60\%$)

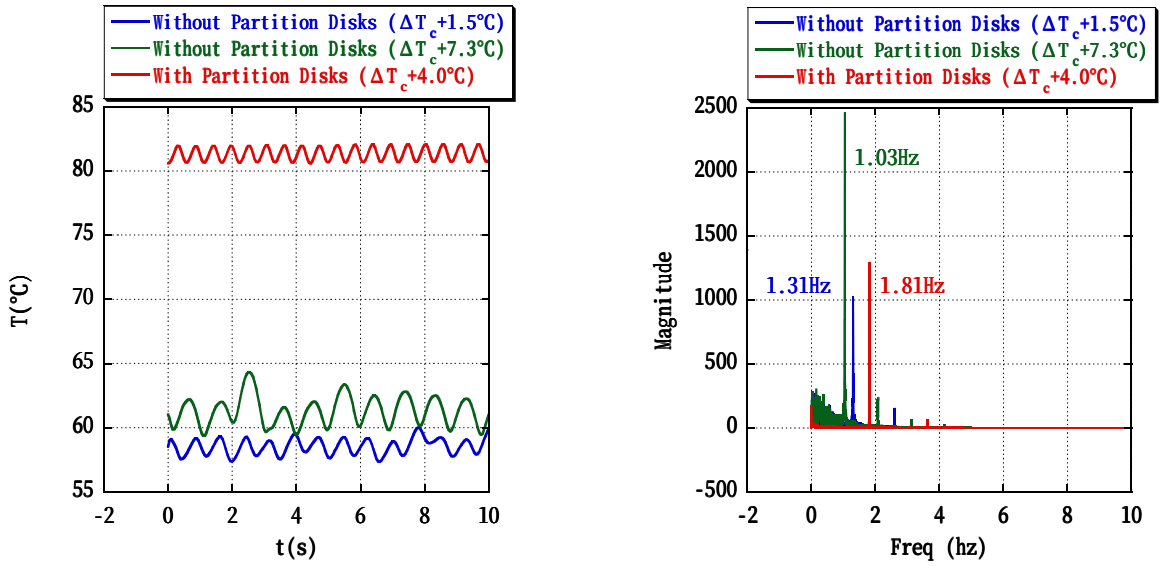

Fig. 3-6 Effect of partition disks over the liquid bridge temperature at steady oscillatory conditions and correspondent FFT analysis ($V/V_0 = 110\%$).

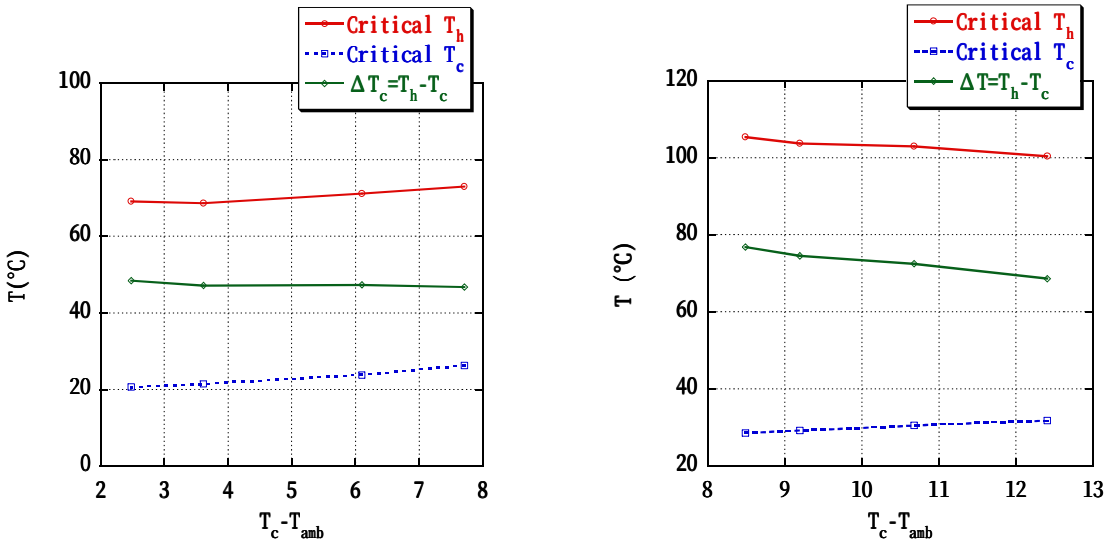

(a) slender liquid bridges ($V/V_0 = 60\%$) (b) nearly flat liquid bridges (V/V_0 = 110%)

Fig. 3-7 Effect of $T_c - T_{amb}$ on the critical temperature difference, ΔT_c.

Similarly to Kamotani (2000), Fig. 3-7 shows the variation of the critical temperature difference, ΔT_c, as function of $T_c - T_{amb}$, where T_c is the cold disk temperature and T_{amb} is the ambient temperature. In the set of experiments shown in Fig. 3-7, T_c is decreased by using the Peltier element cooling, whereas the T_{amb} is maintained almost constant. Fig. 4-7(a) and Fig. 3-7(b) show the results for slender (V/V_0 =60%) and nearly flat liquid bridges (V/V_0 =110%), respectively, both having the partition disks to partially suppress the natural convection effect. It is shown in the figures that the decreasing of of $T_c - T_{amb}$ has a stabilizing effect (increasing of ΔT_c) for $V/V_0 = 110\%$, although exerting little influence for $V/V_0 = 60.0\%$ (near constant ΔT_c).

3.4 Determination of the heat flow through the rods

After determination of the onset of oscillation, in which the temperature difference between the disks, ΔT_c, is increased very slowly, other set of experiments is performed in order to obtain the heat loss from the liquid bridge. In this case, ΔT_c is set constant until steady temperature conditions are obtained. The configuration using the partition disks to suppress partially the natural convection around the liquid bridge is used in all the experiments presented in this section. Fig.3-8 shows a typical supercritical plot as function of time when ΔT is set constant at $\Delta T_c + 4$ °C. The temperature distributions in the upper and lower disk rods for the same conditions shown in Fig.3-8 are shown in Fig.3-9. From these temperature distributions, the heat flow through the rods can be obtained by the procedure described later, and then by subtraction of the upper and lower disk rod heat flows, the heat loss from the liquid bridge can be obtained.

Neglecting the radial temperature variation in the rod, an axial balance of energy through the rod results in the following one dimensional (1-D) expression:

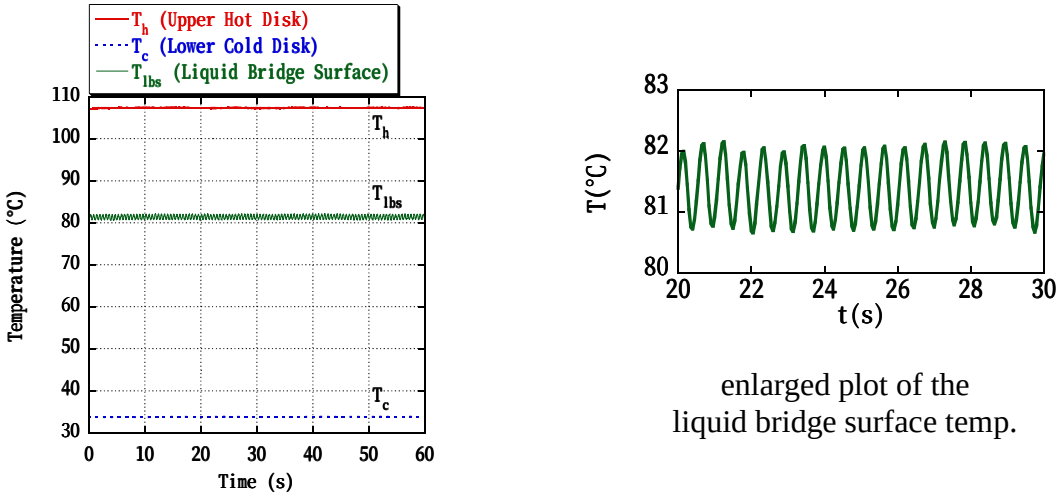

Fig. 3-8 Typical temperature signals at a supercritical ΔT (the same as Fig. 3-2, excepting that $\Delta T = \Delta T_c + 4.0$ °C is kept constant and $T_{amb} = 21.5$ °C).

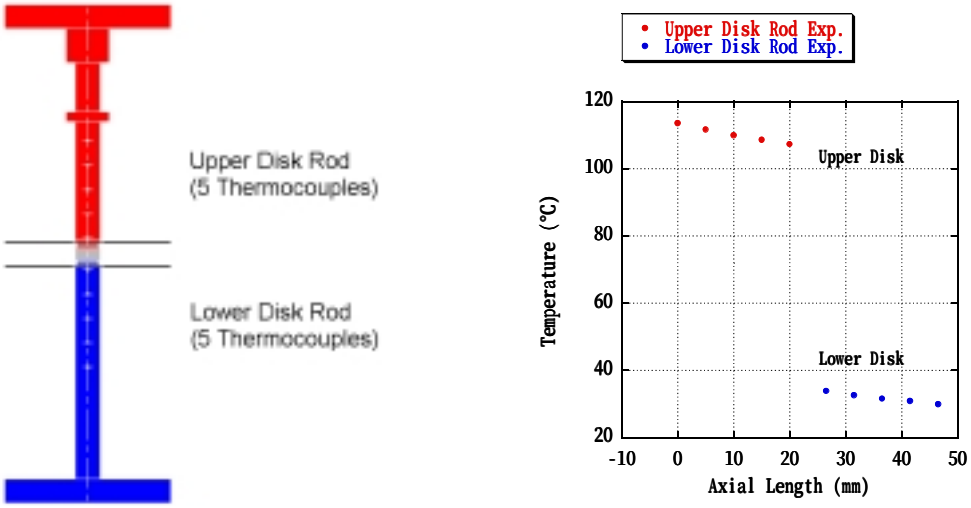

Fig. 3-9 Temperature distributions in the upper and lower rods.

$$\rho C_p A \frac{\partial T}{\partial t} = \frac{\partial}{\partial z}\left(kA \frac{\partial T}{\partial z} \right) - h_{rod\ side} \pi D \left(T - T_{amb} \right) - \varepsilon(\sigma) \pi D \left(T^4 - T_{amb}^4 \right) \qquad (3.2)$$

where ρ is the rod density, C_p the heat capacity, A the rod section area, T the rod temperature, $T_{ambient}$ the ambient temperature, t the time, z the axial distance from the first thermocouple, $h_{rod\ side}$ the heat transfer coefficient at the rod side surface. The second and the third terms in the RHS represent the heat transfer by natural convection and by thermal radiation from the rod surface to the ambient air. Preliminary calculations indicate the radiation heat transfer to be nearly negligible, mainly due to the relatively low emissivity of the aluminum. This term is explicitly included in Eq. (3.2) because of precision reasons.

The boundary conditions can be given by

$$\begin{aligned} T &= T_0 \qquad\qquad at \;\; z = 0 \\ -k\frac{\partial T}{\partial z} &= h_{rod\ end}\left(T - T_{lb}\right) \qquad at \;\; z = L_{rod} \end{aligned} \tag{3.3}$$

where T_{lb} the liquid bridge average temperature and $h_{rod\ end}$ the heat transfer coefficient at the rod end (in contact with the liquid bridge). Eqs. (3.2) and (3.3) are solved by using the finite difference method. $h_{rod\ side}$ is calculated locally from the following relation obtained experimentally for vertical cylinders with uniform surface temperature in laminar flow regime (Fujii & Koyama, 1978):

$$\frac{\left(Nu_z\right)_c}{\left(Nu_z\right)_p} = \frac{\left(h_{rod\ side} z / k_{air}\right)_c}{\left(Nu_z\right)_p} = 1 + 0.43\left[\frac{z / r_o}{\left(Nu_z\right)_p}\right]^{5/6} \tag{3.4}$$

where the local Nusselt number for vertical plates (Holman, 1989), is given by

$$\left(Nu_z\right)_p = 0.508\,\mathrm{Pr}^{1/2}\left(0.952 + \mathrm{Pr}\right)^{-1/4} Gr_z^{1/4}. \tag{3.5}$$

Properties are evaluated at the film temperature (average temperature between the rod and the ambient air), and the Grashof number is defined by

$$Gr_z = \frac{g\beta\left(T_w - T_\infty\right)z^3}{\nu^2}. \tag{3.6}$$

$h_{rod\ end}$ is varied until calculations fit the experimental temperature values. The heat flow through the rod can be obtained by

$$Q_{rod\ end} = h_{rod\ end} A\left(T_{rod\ end} - T_{lb}\right) \tag{3.7}$$

The heat loss from the liquid bridge to the ambient can be determined indirectly by performing the subtraction of the measured values of the heat flows through the upper and lower disks:

$$Q_{heat\ loss} = Q_{upper\ rod} - Q_{lower\ rod} \quad . \tag{3.8}$$

Uncertainty analysis has indicated that the uncertainty associated with the evaluated heat loss is 30% at 99% coverage (see Appendix A).

The Nusselt number due to convection can be calculated by

$$h = \frac{Q_{heat\ loss} - Q_{radiation}}{A_{lbs}\left(T_{lbs} - T_{amb}\right)} \tag{3.9}$$

According to a calculation of the static shape of the free-surface of the liquid bridge under ground based conditions, the liquid bridge surface area, A_{lbs}, as function of the volume ratio for $D = 5.0$ mm and $L = 2.5$ mm is given by

$$A_{lbs} = \pi DL\left[0.3062 + 0.8868(V/V_0) - 0.1927(V/V_0)^2\right] \tag{3.10}$$

This equation is valid for $0.6<V/V_0<1.1$.

Considering the liquid bridge as a body surrounded by a large enclosure, the heat flow due to radiation, $Q_{radiation}$, is given by

$$Q_{radiation} = \varepsilon_{lbs}\sigma A_{lbs}\left(T_{lbs}^4 - T_{amb}^4\right) \tag{3.11}$$

Figure 3-10 shows the measured and the calculated temperature distributions of the upper and lower disk rods for the supercritical condition shown in Fig.3-9. Validation of the method is shown in Appendix B. Figure 3-11 shows the heat flows through the upper disk rod, lower disk rod and liquid bridge surface for V/V_0 = 60% and 110% at various temperature differences between disks, ΔT. The heat loss from the liquid surface increases slightly with increase of ΔT for $V/V_0 = 60\%$, whereas for $V/V_0 = 110\%$ the heat loss remains nearly constant until the onset of oscillation at $\Delta T = 69.4$ °C, then decreases slightly with increase of ΔT. The Biot number, $Bi = h_{lbs}L/k_{oil}$, decreased monotonically with an increase of ΔT .

3.5 Conclusions

An indirect method to determine the heat loss from the liquid bridge was developed and applied successfully to the determination of the Biot number for subcritical, critical and supercritical conditions in a half-floating zone. The range of the present measured *Bi* number is approximately 1-3 (see Fig.3-11). Kuhlmann & Rath (1993) used $B_i = 10$ in their numerical analysis ($Pr = 0.01$-30) and Kamotani (2000) obtained from calculations that $Bi = 0.3$-0.8 for 2-cSt silicone oil, $D = 3$ mm and $L = 1.95$.

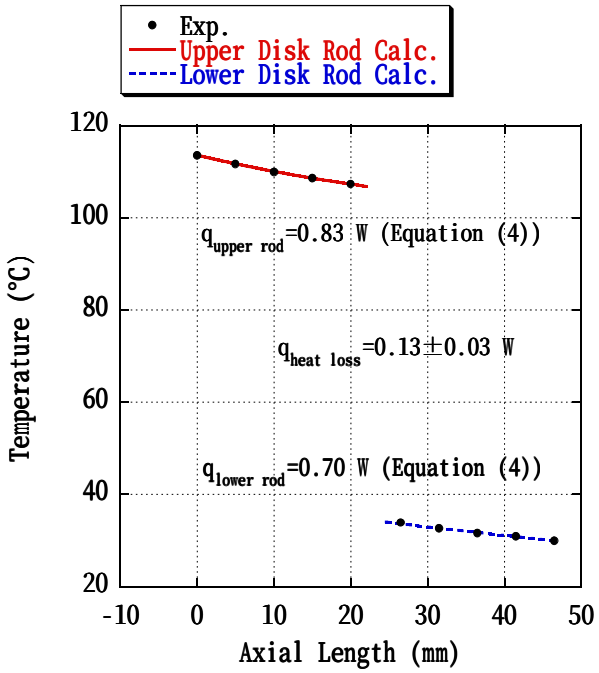

Fig. 3-10. Temperature distributions of the upper and lower disk rods (the same as Fig. 3-9).

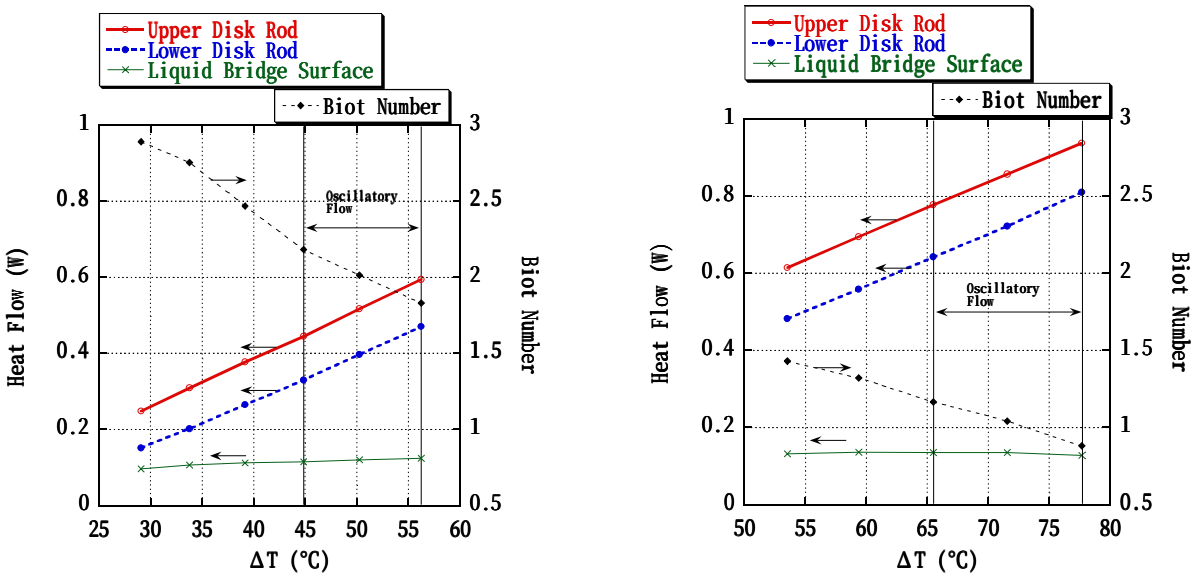

(a) $V/V_0 = 60\%$ (b) $V/V_0 = 110\%$

Fig. 3-11. Biot number and heat flows for various ΔT.

REFERENCES

Antar, B. N and Nuotio-Antar, V. S., 1993, *in* Fundamentals of Low Gravity Fluid Dynamics and Heat Transfer, CRC Press, pp. 31-86.

Fu, B.-I. and Ostrach, S., 1983, Numerical Solutions of Thermocappilary Flows in Floating Zones, *Proceedings of the ASME Winter Meeting*, Boston, Massachusetts, 13-18, pp.1-9.

Fujii, T. and Koyama, S., 1978, Free Convection Heat-Transfer from a Vertical Thin Wire, (in Japanese), *Trans. JSME*, Vol. 44, No. 377, pp.118-125.

Holman, J. P., 1989, Heat Transfer, McGraw-Hill (SI Metric Edition), pp.328.

Kamotani, Y. and Ostrach, S., 1998, Theoretical Analysis of Thermocapillary Flow in Cylindrical Columns of High Prandtl Number Fluids, *Transactions of the American Society of Mechanical Engineers, Journal of Heat Transfer*, Vol. 120, pp. 758-764.

Kamotani, Y., 2000, private communication.

Kawamura, H., 2000, Numerical Simulation of Marangoni Convection in Consideration of Free Surface Deformation (Part 3), *Annual Report of Marangoni Convection Modeling Research (April 1, 1999-March 31, 2000)*, NASDA-TMR-000006E, pp. 181-212.

Kawamura, H., 2001, private communications.

Kozhoukharova, Zh. and Slavchev, S., 1986, Computer Simulation of the Thermocapillary Convection in a Non-Cylindrical Floating Zone, *Journal of Crystal Growth*, Vol. 74, pp. 236-46.

Kuhlmann, H. C. and Rath, H. J., 1993, Hydrodynamic Instabilities in Cylindrical Thermocapillary Liquid Bridges, J. Fluid Mech., Vol. 247, pp.247-274.

Li, J., Sun, J. and Saghir, Z., 1993, Buoyant and Thermocapillary Flow in Liquid Encapsulated Floating Zone, *Journal of Crystal Growth*, Vol. 131, pp. 83-96.

Masud, J., Kamotani, Y. and Ostrach, S., 1997, Oscillatory Thermocapillary Flow in Cylindrical Columns of High Prandtl Number Fluids, *Journal of Thermophysics and Heat*

Transfer, Vol. 11, No. 1, pp. 105-111.

Nishino, K., Kitagawa, T. and Yoda, S., 1999, Experimental study of oscillatory flow and transition behavior of high Prandtl number Marangoni Convection, *NASDA Technical Memorandum (Annual Report of Marangoni Convection Modeling Research)*, NASDA-TMR-990007E, pp. 39-69.

Shevtsova, V. M., Ermakov, M. K., Ryabitskii, E. and Legros, J. C., 1997, Oscillations of a Liquid Bridge Free Surface due to the Thermal Convection, *Proceedings of the 48th International Astronautical Congress*, IAF-97-J.4.02, October 6-10, Turin, Itali.

Smith, M. K. and Davis, S. H., 1983, Instabilities of Dynamic Thermocapillary Liquid Layers. Part 1. Convective Instabilities, *Journal of Fluid Mechanics*, Vol. 132, pp.119-144.

Appendix A - Measurement Uncertainty Associated with Heat Loss Evaluation

(a) Definition of the measurement process

Thermocouple emf / TC (mV) → Connector → MTT Amplifier module / 1000 TC (V) → MTT amplifier base → Keyence NR-110 card → Notebook PC → Software → Data [T(°C) = a (1000 TC) + b) → Filtered data. (a and b are coefficients determined from calibration, otherwise a = 24.0 and b = 0.0).

Experiment (upper & lower rods / with liquid bridge) → Data of 10 thermocouples → Program → Calculation of the heat transfer coefficients from the rod to the ambient air of the upper rod and the lower rod → Determination of the heat transfer coefficients from the upper rod to the liquid bridge & from the liquid bridge to the lower rod → Heat loss.

(b) Listing of elemental error sources

Thermocouple, thermocouple position, amplifier module, base module, Keyence card, notebook PC, data acquisition program, calculation of heat conduction, determination of heat transfer coefficients and curve fitting of rod temperature.

(c) Estimation of elemental errors

Thermocouple: $B_{a,1} = \pm 0.05$ °C, $S_{a,1} = 0.025$ °C, $\nu_{a,1} > 30$

Thermocouple position: $B_{b,1} = \pm 0.01$ °C

Amplifier module - Base module - Keyence card - Notebook PC - Data acquisition program:

$B_{c,1} = \pm 0.1$ °C, $S_{c,1} = \pm 0.05$ °C, $\nu_{c,1} > 30$

Overall temperature measurement:

$$B_T = (B_{a,1}^2 + B_{a,2}^2 + B_{a,3}^2)^{1/2} = (0.05^2 + 0.01^2 + 0.1^2)^{1/2} = 0.11 \text{ °C}$$
$$S_T = (S_{a,1}^2 + S_{a,2}^2 + S_{a,3}^2)^{1/2} = (0.025^2 + 0.05^2)^{1/2} = 0.056 \text{ °C}$$
$$\nu_T > 30$$

Disk area: $B_A = \pm 0.0002$ m, S_A=0 m

Heat transfer coefficient at the end surface of rod (including the effects of uncertainties associated with calculation of heat conduction, determination of heat transfer coefficient at the side surface of rod and curve fitting of rod temperature):

$B_h = 100$ W/m^2/°C, $S_h = 50$ W/m^2/°C, $\nu_h > 30$

(d) Propagation of the bias and precision errors

The equations for the calculation of the heat loss are as follows:

$$Q_{upper\ rod} = h_{upper\ rod} A\left(T_{upper\ disk} - T_{silicon\ oil}\right) \quad \text{(A.1)}$$

$$Q_{lower\ rod} = h_{lower\ rod} A\left(T_{silicon\ oil} - T_{lower\ disk}\right) \quad \text{(A.2)}$$

$$\begin{aligned} Q_{heat\ loss} &= Q_{upper\ rod} - Q_{lower\ rod} \\ &= h_{upper\ rod} A\left(T_{upper\ disk} - T_{silicon\ oil}\right) - h_{lower\ rod} A\left(T_{silicon\ oil} - T_{lower\ disk}\right) \\ &= \left(hA\Delta T\right)_{upper} - \left(hA\Delta T\right)_{lower} \end{aligned} \quad \text{(A.3)}$$

Uncertainties associated with temperature differences are evaluated as:

$$B_{\Delta T} = \left[B_T^2 + B_T^2\right]^{1/2} = (0.11^2 + 0.11^2)^{1/2} = 0.16 \text{ °C} \quad \text{(A.4)}$$

$$S_{\Delta T} = \left[S_T^2 + S_T^2 \right]^{1/2} = (0.056^2 + 0.056^2)^{1/2} = 0.079\ ^\circ\mathrm{C} \tag{A.5}$$

The bias limit of the heat loss may be evaluated as follows:

$$\begin{aligned} B_Q = \Big\{ & \left[(\theta_h B_h)^2 + (\theta_A B_A)^2 + (\theta_{\Delta T} B_{\Delta T})^2 \right]_{upper} \\ & + \left[(\theta_h B_h)^2 + (\theta_A B_A)^2 + (\theta_{\Delta T} B_{\Delta T})^2 \right]_{lower} \Big\}^{1/2}, \end{aligned} \tag{A.6}$$

where $\theta_h = \dfrac{\partial q}{\partial h}$, $\theta_A = \dfrac{\partial q}{\partial A}$ and $\theta_{\Delta T} = \dfrac{\partial q}{\partial \Delta T}$. By using Eq. (A.3), this expression for the bias limit can be simplified and evaluated as follows:

$$\begin{aligned} \frac{B_Q}{Q} &= \left\{ \left[\left(\frac{B_h}{h} \right)^2 + \left(\frac{B_A}{A} \right)^2 + \left(\frac{B_{\Delta T}}{\Delta T} \right)^2 \right]_{upper} + \left[\left(\frac{B_h}{h} \right)^2 + \left(\frac{B_A}{A} \right)^2 + \left(\frac{B_{\Delta T}}{\Delta T} \right)^2 \right]_{lower} \right\}^{1/2} \\ &= \left\{ \left[\left(\frac{100}{1100} \right)^2 + \left(\frac{0.0001}{0.0050} \right)^2 + \left(\frac{0.16}{30} \right)^2 \right] + \left[\left(\frac{100}{950} \right)^2 + \left(\frac{0.0001}{0.0050} \right)^2 + \left(\frac{0.16}{30} \right)^2 \right] \right\}^{1/2} \\ &= 0.14, \end{aligned} \tag{A.7}$$

Similarly,

$$\frac{S_q}{q} = \left\{ \left[\left(\frac{50}{1100} \right)^2 + \left(\frac{0.079}{30} \right)^2 \right] + \left[\left(\frac{50}{950} \right)^2 + \left(\frac{0.079}{30} \right)^2 \right] \right\}^{1/2} = 0.070$$

Note that, since all of the precision indices of the independent parameters are based on experience, meaning that a large number of readings are available, the degrees of freedom can be assumed to be greater than 30, so that the Student-*t* value can be taken to be 2.

(e) Overall uncertainties

Overall uncertainties are evaluated as follows:

$$U_{ADD} = B + tS_{\overline{X}} \qquad \text{(99\% coverage)} \tag{A.8}$$

$$U_{RSS} = \left[B^2 + (tS_{\overline{X}})^2 \right]^{1/2} \qquad \text{(95\% coverage)} \tag{A.9}$$

Therefore,

$$\frac{U_{ADD}}{Q} = \frac{B}{Q} + t\frac{S_{\overline{X}}}{Q} = 0.14 + 2 \times 0.070 = 0.28 \quad \text{(99\% coverage)}$$

$$\frac{U_{RSS}}{Q} = \left[\left(\frac{B}{Q} \right)^2 + \left(t\frac{S_{\overline{X}}}{Q} \right)^2 \right]^{1/2} = \left[0.14^2 + (2 \times 0.070)^2 \right]^{1/2} = 0.20 \quad \text{(95\% coverage)}$$

Appendix B - Validation of the Method for Heat Loss Evaluation

Actual experiments in a liquid bridge have shown the heat loss to be of order of 0.1～0.15 W, and uncertainty analysis given in Appendix A has indicated the uncertainty associated with the evaluated heat loss to be about 30% at 99% coverage. In order to validate the method to measure the heat loss from the liquid bridge presented in this report, a silicone sheet (Shin-Etsu, TC-20BG, 200 μm in thickness) is placed between the upper and the lower disks. The heating power of the upper disk is set constant and steady temperature conditions are obtained. Considering a negligible heat loss from the silicone filler to the environment, similar heat flows through the upper and lower disks are expected. Measured values of temperature and heat flows using the present technique are shown in the table for two different heating powers. Although a zero value should be expected, the heat loss, ΔQ, varied from –0.001 to 0.037 W. This range is consistent with the overall uncertainty given in Appendix A.

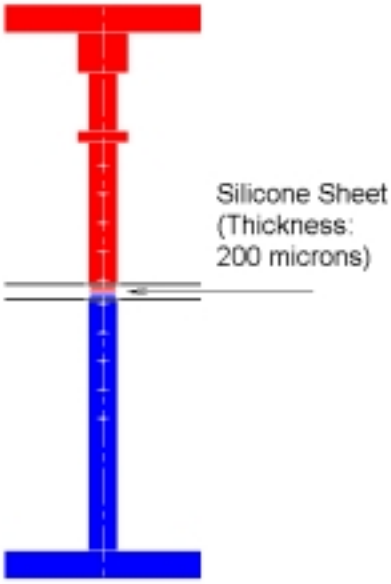

Exp. Num.		1	2
T_1	℃	115.91	44.44
T_2	℃	111.21	43.05
T_3	℃	106.61	41.66
T_4	℃	102.15	40.26
T_5	℃	97.86	38.92
T_6	℃	71.85	31.30
T_7	℃	67.89	30.09
T_8	℃	63.76	28.74
T_9	℃	60.07	27.80
T_{10}	℃	55.93	26.46
T_{amb}	℃	20.48	15.97
Q_{upper}	W	3.125	0.952
Q_{lower}	W	3.127	0.915
ΔQ	W	-0.001	0.037

Fig. A-1 Experimental configuration with a silicone sheet placed between the disks.